Available online at www.sciencedirect.com
ScienceDirect
Trans. Nonferrous Met. Soc. China 34(2024) 2714−2732
Transactions of Nonferrous Metals Society of China
www.tnmsc.cn

Sn nucleation and growth from Sn(II) dissolved in ethylene glycol: Electrochemical behavior and temperature effect

Kiem Van DO[1], Hieu Van NGUYEN[1,2], Tu Manh LE[2,3]

1. Faculty of Electrical and Electronic Engineering, Phenikaa University, Yen Nghia, Ha-Dong, Hanoi 10000, Vietnam;
2. Phenikaa Research and Technology Institute (PRATI), A&A Green Phoenix Group, 167 Hoang Ngan, Hanoi 10000, Vietnam;
3. Faculty of Materials Science and Engineering, Phenikaa Institute for Advanced Study (PIAS), Phenikaa University, Hanoi 10000, Vietnam

Received 5 April 2023; accepted 13 November 2023

Abstract: Thermodynamic and kinetic aspects of Sn nucleation and growth processes onto a glassy carbon electrode from $SnCl_2·2H_2O$ dissolved in ethylene glycol solutions were studied. Typical reduction and oxidation peaks observed in voltammograms have demonstrated the capability of ethylene glycol solutions to electrodeposit Sn. The temperature-dependence of diffusion coefficient values derived from potentiodynamic and potentiostatic studies helped to determine and validate estimations of the activation energy for Sn(II) bulk diffusion. Chronoamperometric results have identified that, the suitable model to describe the early stage of Sn electrodeposition could be composed of Sn three-dimensional nucleation and diffusion-controlled growth and water reduction contributions, which was duly validated by theoretical and experimental approaches. From the model, typical kinetic parameters such as the nucleation frequency of Sn (A), number density of Sn nuclei (N_0), and diffusion coefficient of Sn(II) ions (D), were determined. The presence of Sn nuclei with excellent quality and their structures were verified using SEM, EDX, and XRD techniques.
Key words: Sn; nucleation; growth; ethylene glycol; nucleation kinetics; electrodeposition

1 Introduction

Tin (Sn) has a wide range of applications in various industrial fields such as electronics and food industry because of its non-toxic, soft, and ductile properties. Sn coatings can be esthetically pleasing even when exposed to air and moisture that supply decorative finishes. Besides, the pure Sn coating has also been utilized to form a protective surface to enhance corrosion resistance, resist air oxidation, and improve solderability [1]. In addition, Sn and its alloys have attracted attention to be used as anode materials for Li-batteries as alternatives for graphite and electrocatalysts for electrochemical reduction of CO_2 to HCOOH [2]. Among different methods of Sn synthesis, electrodeposition is known as the most common one with a long history in metallic coating industries [3,4]. This method provides some benefits such as relatively simple synthesis process, low energy consumption, and inexpensiveness [5,6].

Experiences from these works [3−6] have shown that the choice of electrolyte solution plays an important role in the electrodeposition process. Traditionally, several researchers used acidic or alkaline aqueous solutions to electrodeposit Sn and its alloy. Unfortunately, these media were associated

Corresponding author: Tu Manh LE, E-mail: tu.lemanh@phenikaa-uni.edu.vn;
Hieu Van NGUYEN, E-mail: hieu.nguyenvan@phenikaa-uni.edu.vn
DOI: 10.1016/S1003-6326(24)66571-4

with toxic components because alkaline baths are usually hydroxide-based, while acidic baths have sulfate or sulphurated-based compositions [7,8]. Due to the toxicity of these components, in recent years, new alternatives to replace the traditional ones have been developed such as room-temperature ionic liquids (RTILs) and deep eutectic solvents (DESs) based on choline chloride (ChCl). Interesting properties of DESs have attracted significant attention in the field of electrodeposition of metals and their alloys, i.e., Ni, Co and Sn−Zn [9−12].

However, several works have revealed that the presence of water has a pronounced effect on the chemical and thermodynamic properties of DESs [13−16]. It is worth mentioning that high viscosity and low conductivity giving rise to a slow ions diffusion process as well as electrodeposition kinetics could be the main limitations of DESs in particular and nonaqueous solvents in general. To overcome this problem and reduce the impact of residual water, several works have recently focused on removing ChCl, a highly hygroscopic component of the DES, by using a metal chloride salt with the solely ethylene glycol (EG) solvent as an electrolyte solution for the electrodeposition of metals [17−19]. Recently, the direct use of EG has attracted several authors to electrodeposit metals such as Fe and Co by PANZERI et al [19,20] and Ni by PHI et al [21] due to the better quality of deposits, where they verified the vital importance of kinetic study for metal electrodeposition from EG, which is complex due to mixed control of diffusion and migration processes and suggested that the use of NaCl as supporting electrolyte (SE) was necessary to make the system under control by diffusion, which is primordial to apply model-related diffusion regime. But it is not clear how to select the supporting electrolyte ratio in this system. Meanwhile, the electrodeposition of Sn and its alloys from EG has been studied by VOROBYOVA and KUDAKA [22] and MALTANAVA et al [23]. However, these works mainly focused on the massive electrodeposition of metals (long electro-deposition time) at a fixed temperature, while a thorough study on thermodynamic and kinetic aspects of the Sn electrodeposition from EG solutions seems to be scarce.

Therefore, this work aims to investigate the temperature effect on kinetics and mechanisms of the early stage of Sn electrodeposition onto glassy carbon electrode (GCE) from EG solutions using cyclic voltammetry (CV) and chronoamperometry (CA) techniques. Scanning electron microscopy (SEM), energy dispersive spectroscopy (EDX), and X-ray diffraction (XRD) were used to characterize the morphology, chemical composition, and crystal structure of the surface electrodeposit, respectively.

2 Experimental

The electrolyte solution was obtained by adding 50 mmol/L $SnCl_2{\cdot}2H_2O$ (99%, Sigma Aldrich) to the EG (purity ≥ 99%), which was kept magnet-stirring at 323 K for 24 h. The electrochemical tests of the system GCE/Sn(II) in EG with and without 250 mmol/L NaCl were performed by CV and CA techniques at different temperatures (298−333 K). These tests were carried out in a three-electrode electrochemical cell using a VersaSTAT 3, Potentiostat/Galvanostat, coupled to VersaStudio software installed in a PC for experimental control and data collection. IR compensation was performed for all the electro-chemical measurements. The amount of residual water on the Sn(II) electrolyte in EG was measured to be less than 0.3 wt.% by Karl Fischer coulometric titration using a Titrino Coulometer model 756 from Metrohm®. The cell consisted of GCE with a surface area of 0.0707 cm^2 as the working electrode, a graphite bar as a counter electrode (CE), and a silver wire as a quasi-reference electrode (RE). The morphology observation and the elementary analysis of the GCE surfaces were carried out using field emission scanning electron microscopy (FE-SEM HITACHI S4800) and EDX technique, respectively. XRD measurements were performed in a Panalytical Empyrean Diffractometer with a Cu K_α radiation tube to determine the crystal structure of Sn deposits. Furthermore, Raman spectra were obtained, in a (Horiba Scientific) MacroRam™ Raman spectrometer with a 785 nm laser excitation, to characterize chemical species formed in the Sn deposit surface.

3 Results and discussion

3.1 Potentiodynamic characteristics

3.1.1 Influence of SE on CV curves

Figure 1 shows the comparison between the

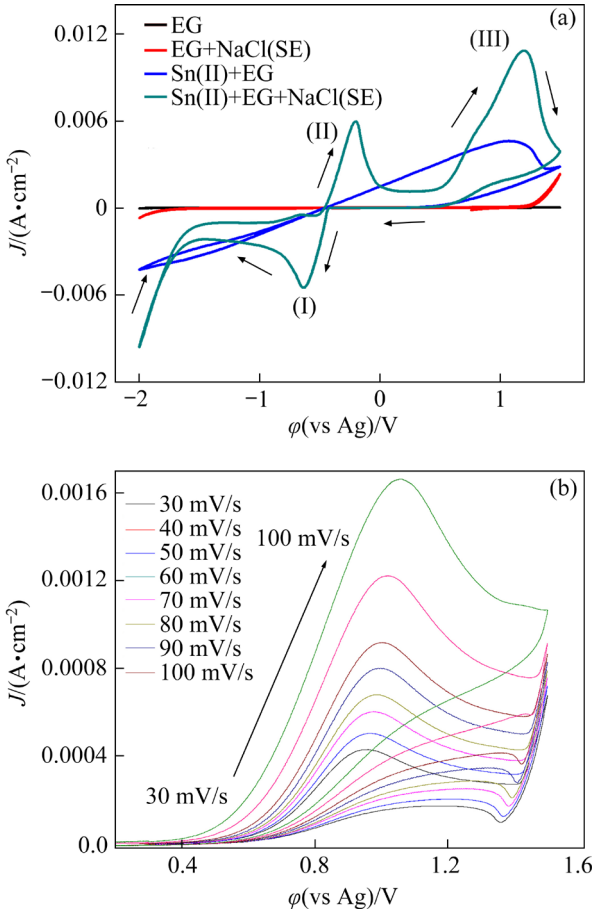

Fig. 1 Comparison of CV curves in different systems of GCE/EG without (black curve) and with (red curve) 250 mmol/L NaCl, and GCE/50 mmol/L $SnCl_2·2H_2O$ dissolved in EG without (blue curve) and with (dark cyan curve) NaCl at scan rate of 50 mV/s (The potential scan was started at 0.15 V in the negative scan direction indicated by arrows) (a), and CV curves of GCE/50 mmol/L Sn(II) in EG with NaCl as SE from 0.2 to 1.5 V at room temperature and scan rate from 30 to 100 mV/s (b)

CV curves in different systems, namely GCE/EG with and without 250 mmol/L NaCl, and GCE/50 mmol/L Sn(II) in EG with and without NaCl, at room temperature. It reveals that the CV curve in the absence of Sn(II) in EG does not exhibit neither oxidation nor reduction peak and its current density is insignificant at a scan rate of 50 mV/s. By adding the SE, within a wide potential range (from −1.75 to 1.25 V) the behavior of CV in EG+SE is similar to that of the black one, while at the potentials of the extremes (i.e., $\varphi \ll -1.75$ V and $\varphi \gg 1.25$ V) the increase in the current density could be due to the decomposition of the solvent favored by the presence of SE ions.

Compared to the previous cases, in the presence of Sn(II) in EG, the CV curve depicts a significant increase in the current density, but the formation of reduction peak is not clearly defined, while in the potential range from −0.2 to 1.4 V the oxidation peak is observed with a widened shape. This could be due to low mobility of the ions in EG during the electrochemical process, producing the migration effect where the process is not fully governed by diffusion control [24]. In this regard, the use of the SE plays an important role in compensating for the migration effect as can be seen in the CV curve recorded in the system GCE/Sn(II)+SE. Thus, the CV curve in the presence of the SE helps the system to clearly form reduction and oxidation peaks in the same potential range as the rest of cases. Moreover, it is important to note that the formation of these (reduction/ oxidation) peaks in the CV curves (blue and dark cyan curves) is associated with the presence of Sn(II) dissolved in each solvent (solely EG or EG+SE) rather than the backgrounds themselves, which contribute a negligible effect to the electrodeposition of Sn from each respective electrolyte solution (EG+Sn(II) or EG+Sn(II)+NaCl). This can be clearly seen in Fig. S1 in Supplementary Materials where CV curves obtained in the system of GCE/50 mmol/L Sn(II) in EG with and without SE after subtracting the background (the CV curve of the systems of GCE/0 mmol/L Sn(II) in EG and GCE/50 mmol/L Sn(II) in EG+SE) remain nearly unchanged.

For the CV curve recorded on the system GCE/Sn(II) in EG with SE, in the forward scan a cathodic peak can be clearly observed in the potential range from −0.4 to −0.82 V, which can be related to the transition state from Sn(II) species to Sn(s), through Reaction (1):

$$\text{Peak I: } Sn(II)_{(EG)}+2e=Sn_{(s)} \quad (1)$$

Correspondingly, in the backward scan the anodic peak (II) located in the potential range from −0.36 to −0.1 V can be associated with the oxidation process of Sn metallic nuclei formed on the electrode surface (see Reaction (1)), occurring through Reaction (2):

$$\text{Peak II: } Sn_{(s)}=Sn(II)_{(EG)}+2e \quad (2)$$

Interestingly, followed by Peak(II) an additional peak appears in the potential range from 0.5 to 1.5 V, corresponding to the oxidation of Sn(II) species to Sn(IV), as presented in Reaction (3):

$$\text{Peak III: } Sn(II)_{(EG)}=Sn(IV)_{(EG)}+2e \quad (3)$$

To confirm the presence of Peak(III), CVs are recorded from 0.2 to 1.5 V as shown in Fig. 1(b). The formation of Peak(III) is evident, independently from another process. Therefore, the second oxidation peak appears due to the oxidation process of Sn(II) species in EG. This observation is consistent with those reported in Refs. [12,25,26].

To examine the influence of the SE on the reduction and oxidation reactions behavior during Sn electrodeposition from EG and NaCl solutions, CV test was carried out at different concentration ratios of NaCl (r), $r=C_{sup}/C_0$=5, 10, 15, 20, and 25, where C_{sup} is the concentration of SE, and C_0 is the concentration of Sn(II). The results are shown in Fig. 2.

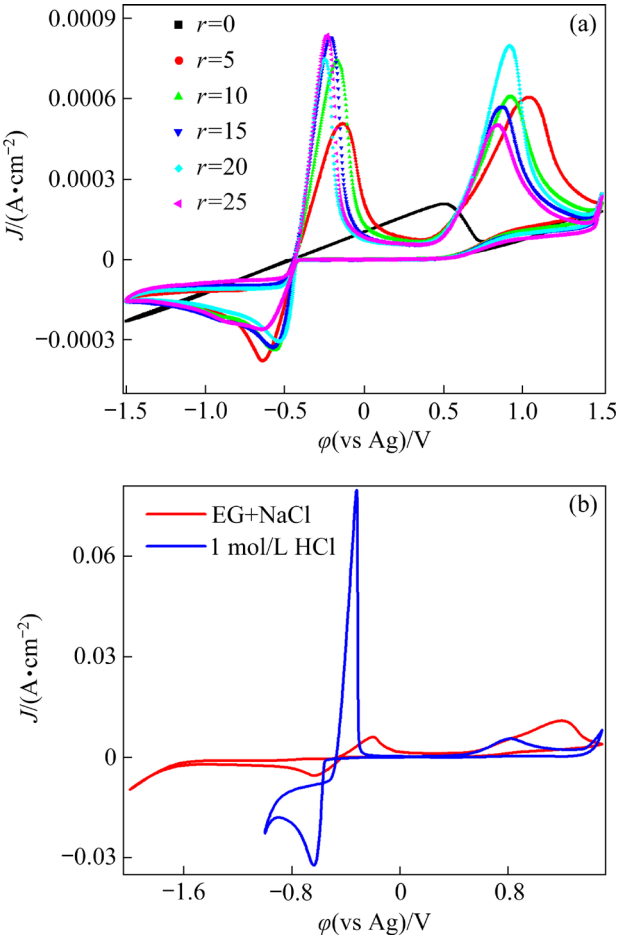

Fig. 2 CV curves in GCE/50 mmol/L Sn(II): (a) With different SE ratios (r=0, 5, 10, 15, 20, 25) in EG at room temperature; (b) With r=5 compared to that recorded in aqueous solvent (1 mol/L HCl)

As mentioned above, there are significant differences between results with and those without SE, thus, with increasing the concentration of NaCl, the reduction peaks tend to shift to more positive potentials (except in the case of r=25), while their intensities gradually decrease with the increase of the NaCl concentration. This effect of the SE is also observed in Ref. [27] for the galvanic deposition of metallic rhenium. It is worth mentioning that when r=25, the SE reaches its saturation concentration, incapable of dissolving more metal salt in EG. The ideal working ratio of SE for the GCE/Sn(II) in EG system should be r=5 since with a similar CV peak shape it has a wider potential window, a lower NaCl concentration, and a better reduction current density compared to the other r values, which is worthy for the Sn electrodeposition.

Another way to assess the effect of the SE is through the cathodic efficiency (η_{CE}, anodic and cathodic charge ratios) as exhibited in Fig. S2 in Supplementary Materials. While the η_{CE} value in the EG solution with the SE goes decreasing from 74.59%, in the absence of SE it gives a higher value of 92.45% (Fig. S2). The decrease in the η_{CE} value could be due to residual water reduction reaction occurring simultaneously during the Sn electrodeposition from the EG solution. This observation is supported by the comparison between the CV curves of Sn(II) in EG with the SE and in 1 mol/L HCl solution, as shown in Fig. 2(b). It reveals that similar reduction and oxidation peaks are formed in acidic solution, but with a reduced electrochemical window. Moreover, there is a huge increase in the current density due to higher mobility of ions and lower viscosity, which increase electrical conductivity, in the aqueous solution compared to EG solutions. However, the η_{CE} value for the aqueous solution was calculated to be 52.67%, which is significantly lower than that of EG solutions. It is worth mentioning that the low η_{CE} value was commonly reported in the acidic or alkaline electrolyte baths since they produce the side reaction (i.e., hydrogen evolution reaction, HER) occurring during the electrodeposition of metals [28]. This result also corroborates that Sn electrodeposition from pure EG is more efficient than those in the presence of the SE and aqueous media. A similar case can be seen elsewhere in Refs. [17,29]. However, the presence of the SE allowed us to apply theoretical models relating diffusion control such as those developed by BERZINS and DELAHAY [30] and SCHARIFKER et al [31−33] for the analysis of the current density transients under the diffusion-controlled process,

respectively. Therefore, the supporting ratio r=5 is appropriate for the present study.

3.1.2 Influence of potential scan rate

Figure 3(a) shows a family of CV curves recorded in the GCE/50 mmol/L Sn(II) system in EG with 250 mmol/L NaCl at different potential scan rates. A reduced potential window compared to Figs. 1 and 2 was used to better visualize the electrochemical behavior of Sn(II) in the studied system. It can be observed that the shape of oxidation and reduction peaks is well-defined. On the other hand, Fig. 3(b) clearly indicates that the cathodic peak current density (J_{cp}) increases linearly with the square root of the potential scan rate ($v^{1/2}$), as described by the Berzins−Delahay equation (see Eq. (4)) [30]. These observations suggest that the Sn electrodeposition in the studied system takes place through a diffusion-controlled process.

$$J_{cp}=\frac{0.61(Fn)^{3/2}C_0(Dv)^{1/2}}{(RT)^{1/2}} \quad (4)$$

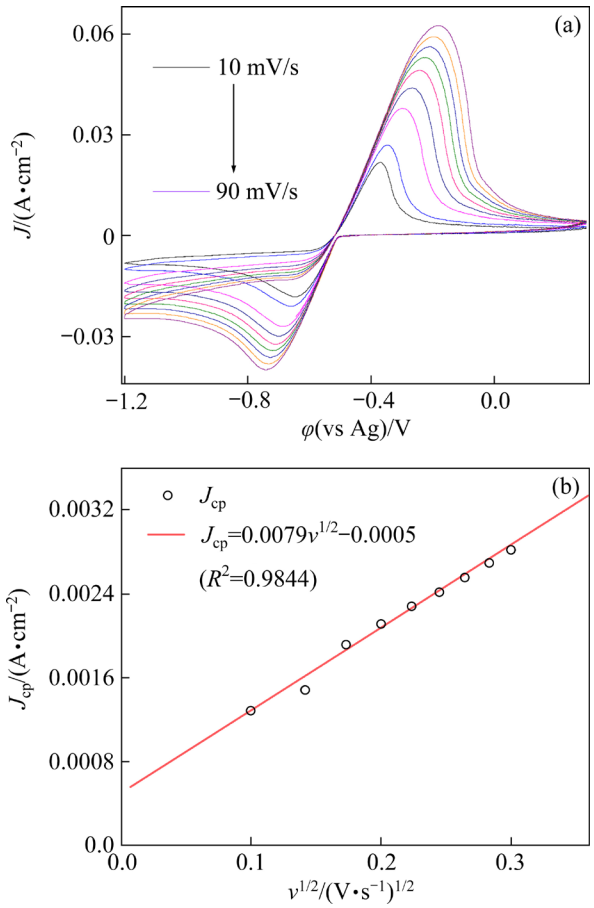

Fig. 3 CV curves of 50 mmol/L Sn(II) in EG with NaCl at room temperature and scan rates from 10 to 90 mV/s (a), and cathode peak current density (J_{cp}) plotted as function of square root of scan rate ($v^{1/2}$) at 298 K (b)

where F (=96480 C/mol) is the Faraday constant, n is the total number of electrons transferred during the electrochemical process, C_0 (mol/L) is the Sn(II) bulk ion concentration, D (cm^2/s) is the diffusion coefficient of Sn(II) ions in EG, R (=8.314 J/(mol·K)) is the thermodynamic gas constant, and T (K) is the thermodynamic temperature. Therefore, further analyses of the Sn electrodeposition process can be performed using theoretical models in fully developed diffusion-controlled regime. From Eq. (4) and the slope of fitting equation in Fig. 3(b), considering the number of electrons transferred n=2 in Reaction (1), the diffusion coefficient D of Sn(II) ions in EG with the SE can be calculated for the studied temperature (298 K).

3.1.3 Influence of temperature

Figure 4(a) shows the CV curves recorded on the GCE of 50 mmol/L Sn(II) in EG with SE at several temperatures (298, 313, 323 and 333 K) to assess the thermodynamic and kinetic behavior of the system. It can be observed that the CV curves shift towards more positive potentials and the current densities increase with the rise of the temperature. The growth in the intensity of current densities is evident on the reduction peaks, while the oxidation one does not follow this trend, but it is out-of-scope of this study. This means that the Sn electrodeposition is favored in terms of the applied potential (φ) with the increase of temperature. This can be explained because the viscosity of EG solutions decreases with the rise of the temperature, while their electrical conductivity increases. Simultaneously, the temperature increase gives rise to the increase of the kinetic energy via thermal vibration of the ions present in the solution that improves the mobility of Sn(II) ions. Thus, the Sn(II) electrodeposition potential is less affected by the polarization, leading to the positive shift of the reduction peak [34].

The temperature effect in kinetics of Sn electrodeposition can be studied through the relationship with the diffusion coefficient D as shown in Fig. 4(b) by plotting J_{cp}–$v^{1/2}$ curves at different temperatures. According to Ref. [35], the dependence of D on temperature can be determined by

$$D(T)=D_0\exp[-\Delta E^0/(RT)] \quad (5)$$

By taking the natural logarithm on both sides of Eq. (5), it can be rewritten as

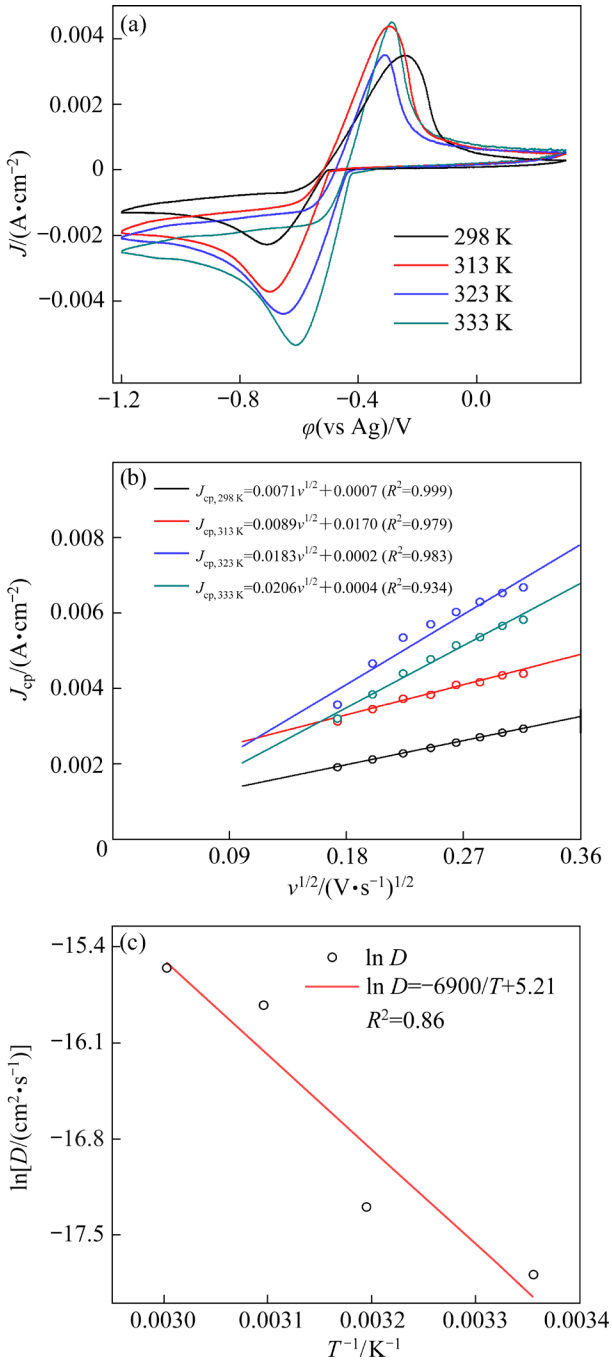

Fig. 4 CV curves of GCE/50 mmol/L Sn(II) with 250 mmol/L NaCl in EG at different temperatures and potential scan rate of 50 mV/s (a), J_{cp} as function of square root of scan rate at different temperatures (b), and temperature dependence of D ($\ln D$ vs $1/T$) from CVs using data obtained in Table 1 (c)

$$\ln[D(T)]=-\frac{\Delta E^0}{R}\frac{1}{T}+b \quad (6)$$

where ΔE^0 is the activation energy for bulk diffusion, D_0 is a preexponential factor, and b is a constant.

Similar to the procedure given in Section 3.1.2, using Eq. (4) and the slopes of Fig. 4(c), the values of D at different temperatures are calculated, as shown in Table 1. This temperature dependence of D can help us to determine important thermodynamic parameters such as the activation energy (ΔE^0).

Table 1 Diffusion coefficients of Sn(II) ions at different temperatures calculated from CVs using Eq. (4)

T/K	298	313	323	333
D/(cm²·s⁻¹)	1.88×10^{-8}	3.08×10^{-8}	1.34×10^{-7}	1.76×10^{-7}

From Table 1, it can be seen that the values of D are consistent with those reported in other works [17,20] for the similar EG-based solutions. Moreover, D values in Table 1 increase gradually with the rise of the temperature. From Eq. (6) by plotting $\ln D$ vs $1/T$ and fitting with data given in Table 1, one can estimate ΔE^0 through the slope of the linear fit, as shown in Fig. 4(c). Using the slope of Fig. 4(c) obtained from CV curves, the value of activation energy, ΔE^0, for Sn(II) bulk diffusion is (57.4±13.2) kJ/mol, with an average value of $D=8.99\times10^{-8}$ cm²/s. The large deviation of the ΔE^0 estimated from the correlation coefficient value R^2 of 0.86 in the linear fit (see Fig. 4(c)) could be due to experimental error. It is important to note that this ΔE^0 value is higher than that reported by BAKKALI et al [36] (ΔE^0=23.61 kJ/mol) for Sn electrodeposition from H_2SO_4 solution, with higher average value of diffusion coefficient ($D=1.18\times10^{-6}$ cm²/s). But it is consistent to Eq. (6), in the sense that the smaller the D value, the larger the ΔE^0 value. The higher viscosity of EG solution could also contribute to the large value of the ΔE^0 [37]. It is worth mentioning that the thermodynamic potential has not yet been reported in the literature for tin electrodeposition process in the studied medium. Therefore, to verify this value, a different method to calculate ΔE^0 based on CA curves will be proposed as shown in the next section of the present work.

3.2 Potentiostatic characteristics

3.2.1 Influence of temperature

From CVs (Fig. 4(a)), experimental current density transients (J–t plot, where t is time) of the

GCE/Sn(II) in EG were selected in a proper applied potential range at each corresponding temperature. To assess the effect of the temperature on the Sn electrodeposition, the *J*–*t* plots are recorded at different temperatures (298, 303, 313 and 323 K), as shown in Fig. 5.

According to ISAEV et al [38], the electrodeposition process is considered under diffusion-controlled growth when the CA curves present the fusion of the final segments at different applied potentials, which is associated with overlapping of diffusion zones. This typical character is clearly presented in the CA curves from t>3 s as shown in Fig. 5. Moreover, Cottrell analyses [31,39] performed for the long deposition time after the maximum peak of the CA curves shown in Fig. S3 and Table S1 in Supplementary Materials have confirmed the diffusion-controlled behavior of the Sn electrodeposition from EG solutions. This behavior also indicates that the experimental CA curves can be analyzed by diffusion formalisms such as Scharifker−Hills (SH) models [32].

To determine the governed nucleation types (instantaneous or progressive), non-dimensional analysis was performed by normalizing through their respective time and current density maxima point (t_m, J_m), to compare the experimental data with theoretical plots, using SH models as given in Eq. (7) (for instantaneous nucleation) and Eq. (8) (for progressive nucleation) [32]:

$$\left(J/J_m\right)^2 = 1.9542\left(t/t_m\right)^{-1} \cdot \left(1-\exp\left[-1.2564\left(t/t_m\right)\right]\right)^2 \quad (7)$$

$$\left(J/J_m\right)^2 = 1.2254\left(t/t_m\right)^{-1} \cdot \left(1-\exp\left[-2.3367\left(t/t_m\right)^2\right]\right)^2 \quad (8)$$

From Fig. 6, it can be observed that at t/t_m > 2.5 the non-dimensional plots of experimental CA curves reside out of the validated zone of the SM model. According to PALOMAR-PARDAVÉ et al [35], this part of the normalized CA curve is due to the contribution of a side reaction occurring simultaneously with the Sn electrodeposition from Sn(II) in EG+SE system. Thus, the water added along

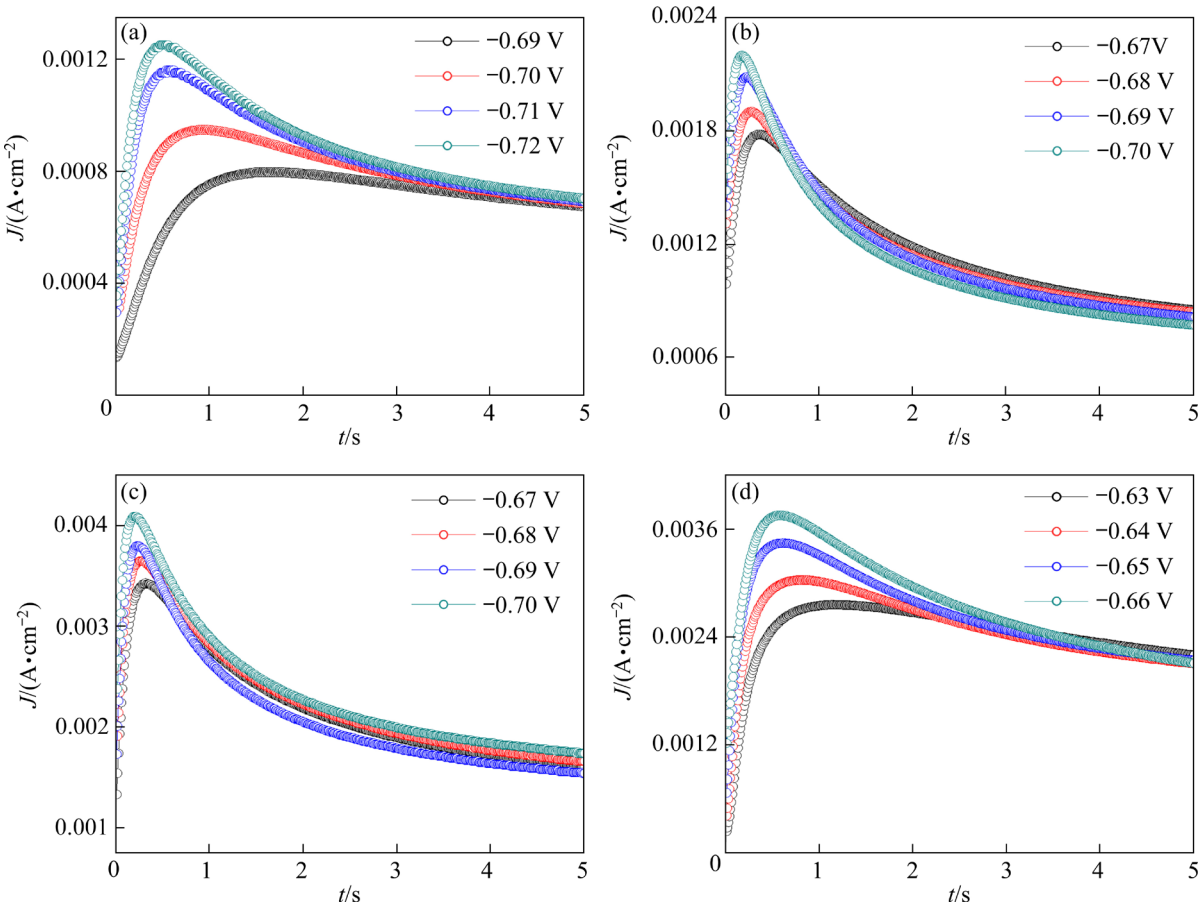

Fig. 5 Experimental potentiostatic current density transients of GCE/50 mmol/L Sn(II) in EG with 250 mmol/L NaCl at different temperatures: (a) 298 K; (b) 313 K; (c) 323 K; (d) 333 K

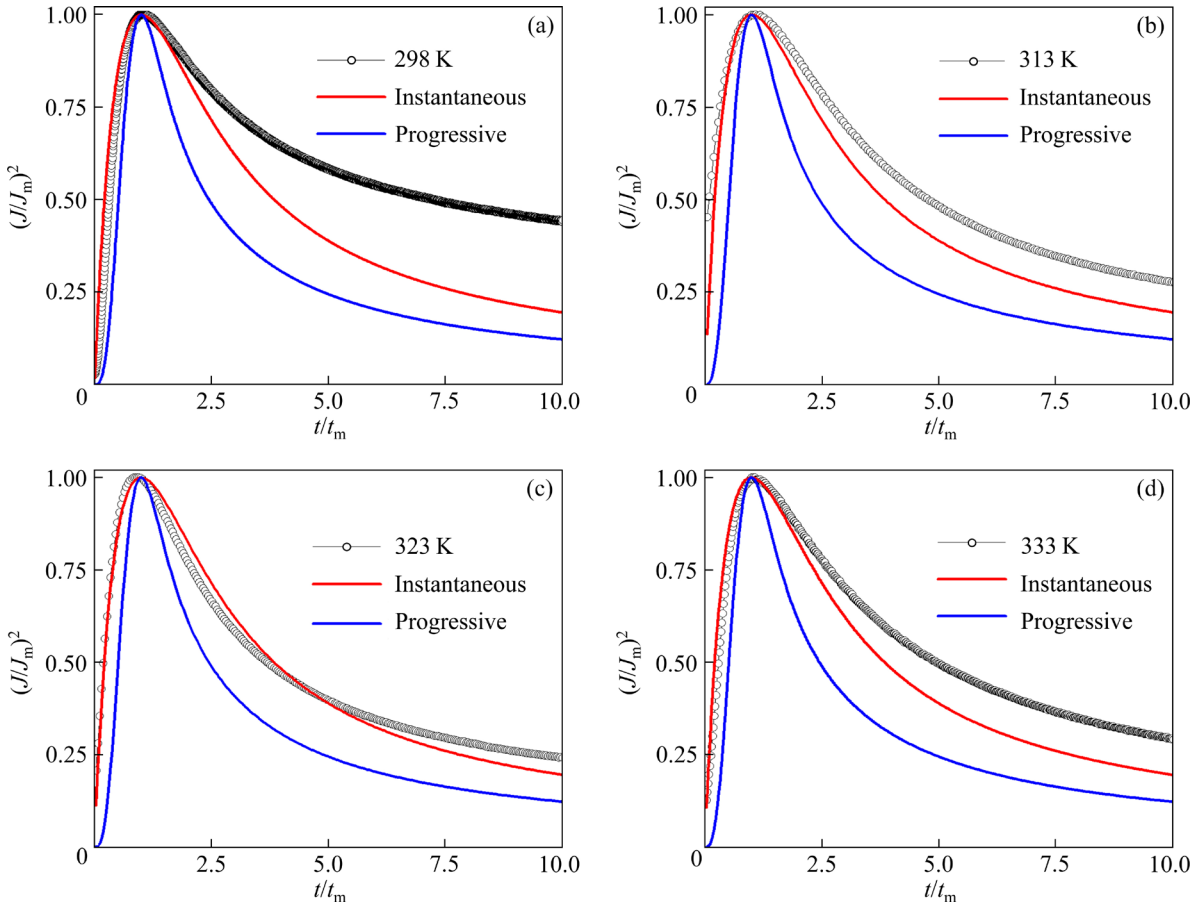

Fig. 6 Experimental non-dimensional plots (black line) of CA in GCE/50 mmol/L Sn(II) in EG with 250 mmol/L NaCl at different temperatures with theoretical ones for instantaneous (red) and progressive (blue) nucleation using Eqs. (7) and (8), respectively: (a) 298 K; (b) 313 K; (c) 323 K; (d) 333 K

with NaCl, which is very hygroscopic, could be electrochemically reduced by Reaction (9) due to the presence of Sn nuclei on the surface electrode acting as a catalyst.

$$2H_2O_{(EG)}+2e_{(Sn)} \rightleftharpoons H_{2(EG)} + 2OH^-_{(EG)} \quad (9)$$

Therefore, the behavior of CAs can be described by a model considering two contributions, which simultaneously occur, to the total current density, namely: (1) 3D nucleation and diffusion controlled-growth of metallic aggregates (J_{3D}), and (2) a faradaic process involving, in this case, water reduction (J_{WR}), on the surface of growing metallic nuclei, as given by Eq. (10) [35]:

$$J_{total}(t)=J_{3D}(t)+J_{WR}(t) \quad (10)$$

where

$$J_{3D}(t)=P_1 t^{-1/2}\left\{1-\exp\left[-P_2\left(t-\frac{1-\exp(-P_3 t)}{P_3}\right)\right]\right\} \quad (11)$$

$$J_{WR}(t)=P_4\left\{1-\exp\left[-P_2\left(t-\frac{1-\exp(-P_3 t)}{P_3}\right)\right]\right\} \quad (12)$$

with

$$P_1=\frac{zFD^{1/2}C_0}{\pi^{1/2}} \quad (13)$$

$$P_2=\pi N_0 D\left(\frac{8\pi MC_0}{\rho}\right)^{1/2} \quad (14)$$

$$P_3=A \quad (15)$$

$$P_4=\left(\frac{2C_0M}{\pi\rho}\right)^{1/2} z_{WR}Fk_{WR} \quad (16)$$

where z is the molar charge transferred during Sn deposition, ρ is the density of the Sn deposit, M is the relative atomic mass of Sn, N_0 is the number density of active sites (Sn nuclei) on the electrode surface, A is the nucleation frequency per active site, z_{WR} is the number of electrons transferred during the water reduction reaction, and k_{WR} is the rate

constant of the water reduction reaction on the Sn deposit surface.

Therefore, Eq. (10) can be parameterized as follows:

$$J(t)=(P_4+P_1t^{-1/2})\cdot\left\{1-\exp\left[-P_2\left(t-\frac{1-\exp(-P_3t)}{P_3}\right)\right]\right\} \quad (17)$$

Figure 7 shows the comparison between the experimental J–t plots and the theoretical ones using Eq. (17) at different temperatures. It can be observed that there is no significant error between the theoretical plots with the experimental ones. This agreement validates that Eq. (17) can fit well to experimental data for different applied potentials and temperatures. On the other hand, from the fitting, some kinetic parameters such as A, N_0, and D can be calculated as given in Table 2. It can be seen from Table 2 that the values of products AN_0 increase (exponentially) with the rise of the potential for each temperature. According to Refs. [31,35,37], the observed behavior of the product AN_0 is suitable to confirm the use of the proposed model to fit experimental data. The influence of water reduction on electrodeposition process is evident, as shown in Fig. 8(a), which provides the separation of individual contribution to the total current density transients.

Moreover, the values of D in Table 2 are also consistent with those obtained from the CV method. Using the average values of D in Table 2 for the potentials at each temperature and applying Eq. (6), ΔE^0 can be estimated through the slope of Fig. 8(b) plotted by CA fitting. Thus, ΔE^0 derived from CA method was determined to be (58.1±6.9) kJ/mol, which is consistent with that calculated from CV curves as mentioned above. These results verify the use of the Palomar−Pardave model to analyze and explain the experimetal CA curve of Sn(II) in EG system.

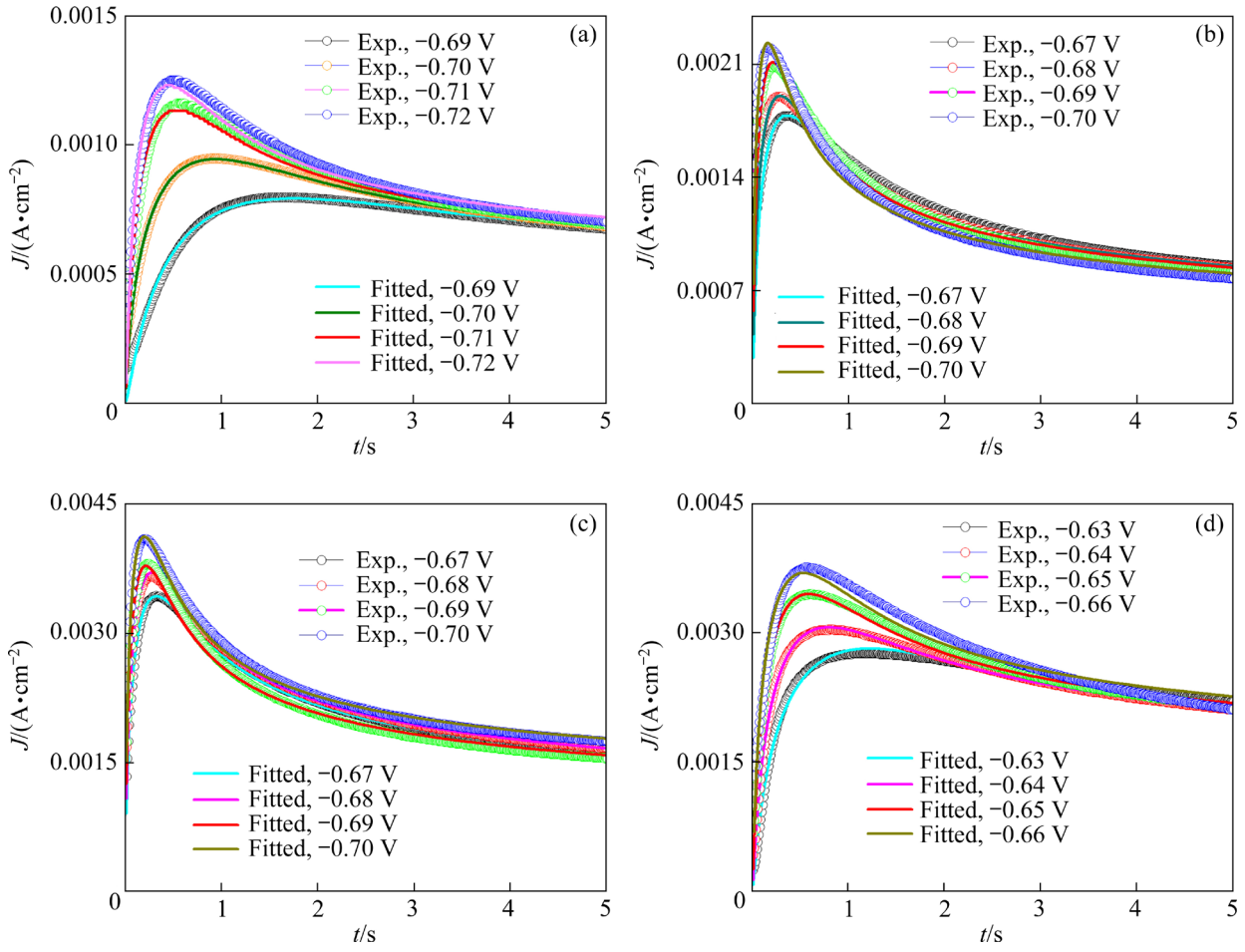

Fig. 7 Comparison between J–t plots of experimental CA results in GCE/50 mmol/L Sn(II) in EG with NaCl and theoretical ones (solid lines) after subtracting induction time at different temperatures: (a) 298 K; (b) 313 K; (c) 323 K; (d) 333 K

Table 2 Best-fit parameters obtained after fitting Eq. (17) to experimental CA curves at different temperatures

T/K	φ/V	P_1/ (10^{-4} A·s$^{1/2}$·cm^{-2})	P_2/s^{-1}	P_3/s^{-1}	P_4/ 10^{-4} s^{-1}	N_0/ 10^8 cm^{-2}	D/ (10^{-8} cm^2·s^{-1})	AN_0/ (10^9 s^{-1}·cm^{-2})
298	−0.69	7.497	1.205	18.346	3.418	1.563	1.897	2.867
	−0.70	7.360	2.021	96.673	3.543	2.719	1.828	26.293
	−0.71	6.926	3.602	56.144	3.952	5.473	1.619	30.730
	−0.72	7.197	4.167	60.080	3.965	5.864	1.748	35.231
313	−0.67	11.741	4.283	190.478	3.275	2.2564	4.652	43.129
	−0.68	11.160	5.377	326.937	3.502	3.146	4.203	102.864
	−0.69	10.902	7.176	356.347	3.513	4.400	4.011	156.802
	−0.70	10.061	9.565	428.809	3.534	6.884	3.416	295.190
323	−0.67	20.825	4.796	950.902	6.878	8.061	14.635	76.649
	−0.68	21.200	5.495	1200.235	7.100	8.911	1.517	106.956
	−0.69	18.772	7.274	1115.430	7.384	15.045	11.892	167.812
	−0.70	18.900	8.036	8133.730	9.259	16.396	12.054	1333.620
333	−0.63	24.184	1.615	42.101	11.019	20.111	19.740	0.847
	−0.64	22.068	2.418	56.665	11.402	36.192	16.434	2.051
	−0.65	22.555	3.148	92.826	11.757	45.102	17.168	4.185
	−0.66	23.500	3.426	102.269	12.100	45.211	1.864	4.624

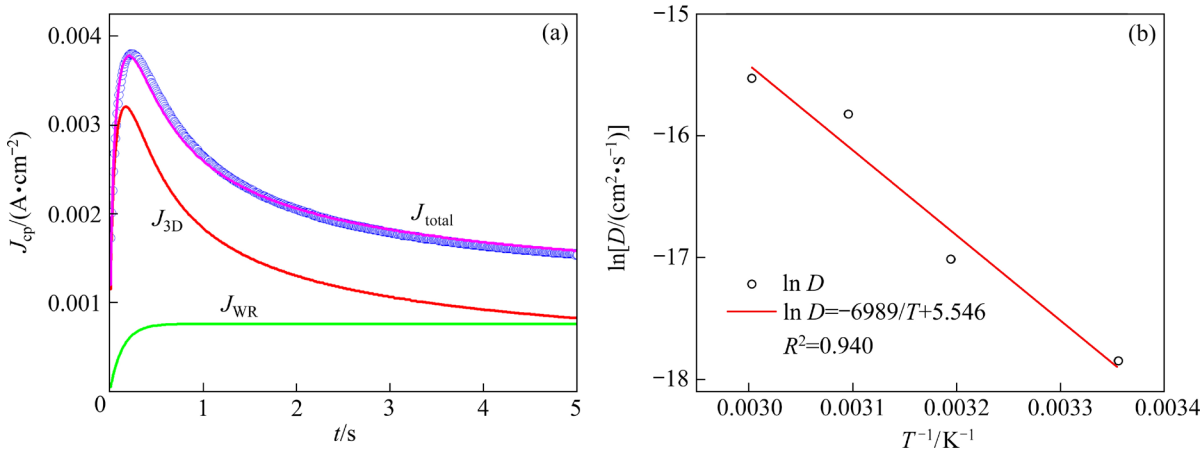

Fig. 8 Separation of individual contribution (J_{3D} and J_{WR}) to total current density transient at applied potential of −0.69 V and 323 K (a), and temperature dependence of D using Eq. (6) from CA method (b)

3.2.2 Sn nucleation and growth in aqueous solvent

Figure 9(a) depicts a family of CA curves recorded on the GCE/Sn(II) in 1 mol/L HCl solution at 298 K. It can be clearly seen that the HCl solution starts to form Sn nuclei at a lower applied potential (φ=−0.55 V) and its CA curves obtained present much larger current densities compared to the those obtained from EG solutions in Fig. 5(a). This verifies a faster kinetics of Sn electro deposition from HCl solutions than from EG solutions. By applying the SH models (see Eqs. (7) and (8)), Fig. 9(b) reveals a similar behavior with those observed from EG due to the contribution of the proton reduction reaction, thus, at t/t_m>2.5, the non-dimensional plot (black curve) of experimental CA curves goes out of the validated region of the SM model bounded by red and blue curves. Therefore, Eq. (17) should be used to obtain kinetic parameters of Sn from acidic solution. Excellent fitting results can be observed in Fig. 9(a) with the best-fit parameters shown in Table S2 in Supplementary Materials. From Table S2, it can be

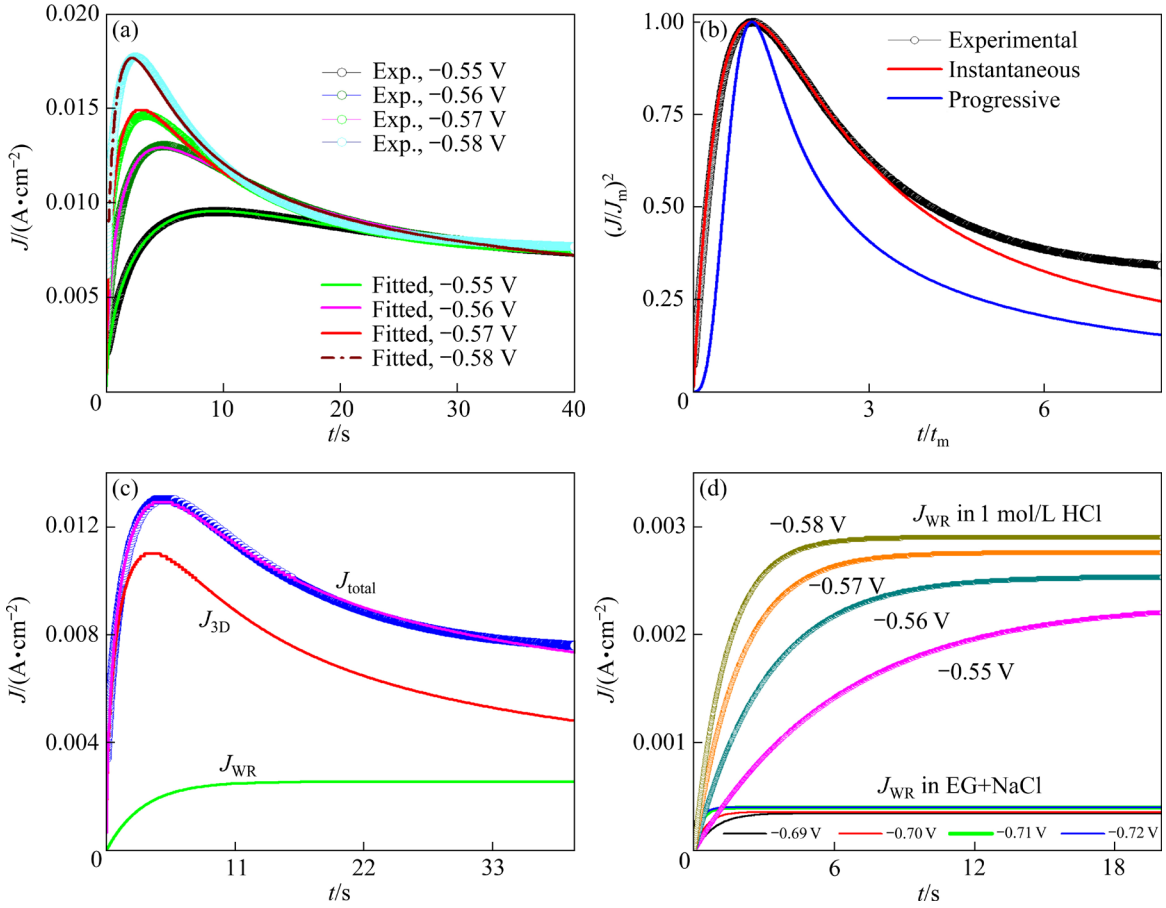

Fig. 9 (a) Experimental CA curves recorded on GCE/Sn(II) in 1 mol/L HCl solution; (b) Comparison of experimental non-dimensional plot (black line) of CA curves at −0.56 V depicted in (a) with theoretical ones for instantaneous (red) and progressive (blue) nucleation using Eqs. (7) and (8), respectively; (c) Separation of individual contribution to total current density transient at −0.56 V and 298 K; (d) Comparison between J_{WR} of Sn(II) in EG+NaCl and HCl solutions at 298 K

seen that the average value of diffusion coefficient of Sn(II) in 1 mol/L HCl solution was calculated to be 2.95×10^{-5} cm^2/s, which agrees with reports in aqueous media [40]. This value is much larger than those obtained from EG solutions. However, the AN_0 product derived from 1 mol/L HCl solution is smaller than that from EG, indicating that the number of Sn nuclei formed at a given electrodeposition time from HCl solution is smaller than that from EG since the effect of water reduction reaction is significant in aqueous solvent. This can be supported by comparing the J_{WR} contributions obtained from HCl and EG solutions in Figs. 8(a) and 9(c). From Fig. 9(d), the J_{WR} value in HCl solution is about 10 times larger than that in EG solution. Moreover, it is clear from Table S2 in Supplementary Materials that the higher the applied potential, the greater the influence of water. The high J_{WR} contribution also affects the efficiency of the electrodeposition due to the liberation of hydrogen as reported in Refs. [28,31,35]. This is also the reason why the use of EG solution for Sn electrodeposition should be a better alternative.

3.3 SEM images

The nucleation process of Sn in EG solutions with and without SE was investigated at distinct concentrations and applied potentials. Figure 10 displays SEM images obtained on GCE surface after Sn nucleation process for 40 s from pure EG solution. It clearly reveals the formation of metallic Sn nuclei with high-resolution image on the GCE surface, confirming the ability of EG solutions to electrodeposit metals. The morphology of Sn crystals changes with the Sn(II) concentration from the pill-shape (50 mmol/L) to a like benzene-shape (100 mmol/L), as can be seen in Figs. 10(b), and (d), respectively. Using only EG solution is an effective

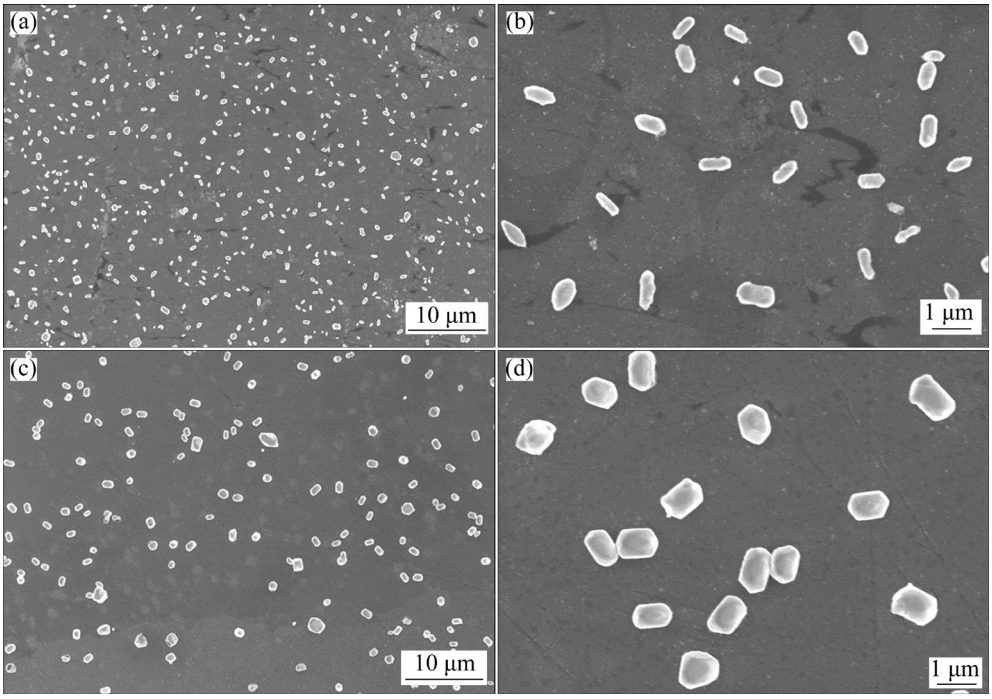

Fig. 10 SEM images of Sn electrodeposited on GCE surface in EG for 40 s at room temperature and −1.0 V from Sn(II) solutions with different concentrations: (a, b) 50 mmol/L; (c, d) 100 mmol/L

way to synthesize Sn particles with high purity, which is worthy in tin electroplating industries.

On the other hand, Fig. 11 shows SEM images taken on the GCE surface after the Sn nucleation process for 40 s from the mixture solutions of 50 mmol/L Sn(II) and EG with 250 mmol/L NaCl at −0.69 V (Figs. 11(a, b)) and −0.72 V (Figs. 11(c, d)). With increasing the potential from −0.69 V (Fig. 11(a)) to −0.72 V (Fig. 11(c)), the morphology of Sn particles (under the film) changed from the spherical shape to the pill-like shape. The distributions of Sn nuclei in Fig. 11 are relatively homogenous. This result suggests that the Sn nucleation on the GCE surface follows the instantaneous nucleation type.

For the sake of comparison between the Sn electrodeposition from EG and aqueous solutions, Figs. 11(e, f) clearly depict SEM images of Sn nuclei electrodeposited from Sn(II) in 1 mol/L HCl solution. Some important issues can be remarked as follows: (1) the sizes of these nuclei are significant smaller than those obtained from EG solution, corroborating the faster kinetics of the Sn electrodeposition from aqueous solution as previously compared from the CA analyses in Figs. 7 and 9; (2) the number density of Sn nuclei is small and the distribution of Sn particles is not homogenous on the electrode surface; (3) significant number of bubbles are formed on the surface during the electrodeposition, reducing the adherence of the deposit with the electrode surface. These issues are evidence of low cathodic efficiency and consequence of the effect of water on the Sn electrodeposition from aqueous media.

Figure 12 shows the comparison between EDX spectra obtained on the GCE surface after the Sn electrodeposition process from EG solution with (Figs. 12(a, b)) and without (Figs. 12(c, d)) NaCl, and from 1 mol/L HCl solution (Figs. 12(e, f)). Sn and C peaks appeared in Fig. 12 clearly indicate the presence of the Sn crystal nucleation on the GCE surface from EG. Interestingly, O peak appears with lower intensity in the case of EG solution without NaCl compared to that with NaCl (Figs. 12(c, d)) and 1 mol/L HCl solution (Figs. 12(e, f)), indicating the clear effect of water during Sn electro-deposition.

It can be seen in Fig. 11 that the Sn particles electrodeposited in the presence of SE on the GCE surface seem to be covered by a thin oxide layer, since they exhibit lower resolution and fuzzy image quality compared to Fig. 10. This film could be SnO_2, which is created during the electrodeposition as consequence of the reaction occurring between

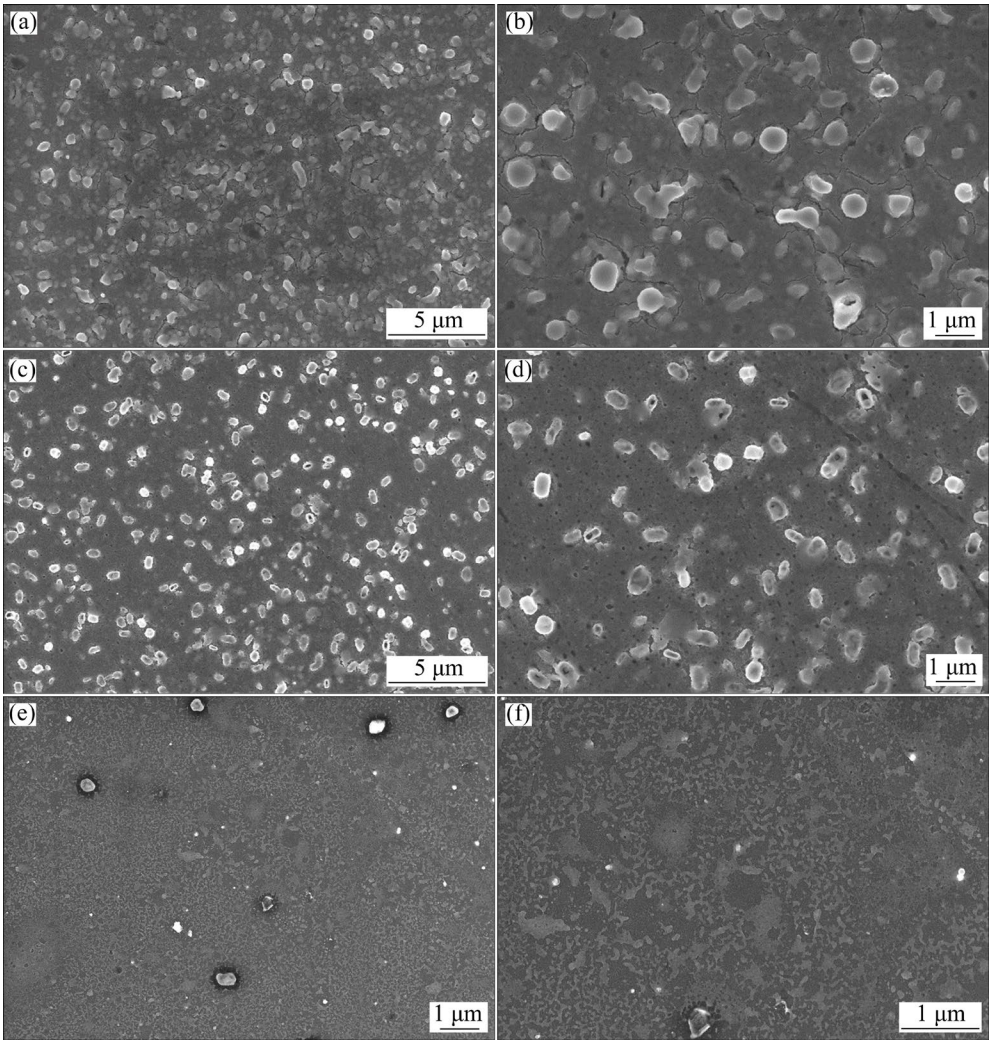

Fig. 11 SEM images of Sn nuclei on GCE surface for 40 s at room temperature from 50 mmol/L Sn(II) in EG with 250 mmol/L NaCl at −0.69 V (a, b) and −0.72 V (c, d), and from 1 mol/L HCl at −0.56 V (e, f)

Sn(II) and OH^- ions provided from the effect of water as demonstrated above in the potentiodynamic study (Reaction (9)), which has also been reported in Refs. [17,28,37]. In a complex manner, the formation of this film could occur via Reaction (18) [28]:

$$2Sn^{2+}+O_2+6H_2O=4H^++2Sn(OH)_4= 2SnO_2\cdot xH_2O+(4-2x)H_2O \quad (18)$$

To verify this observation, Raman spectrum of the Sn electrodeposit onto copper substrates (Fig. S4 in Supplementary Materials) was measured. The characteristic peaks of SnO_2 were observed at 497 cm^{-1}(E_g), 624 cm^{-1}(A_{1g}) and 739 cm^{-1}(B_{2g}) related to the expansion and contraction vibration modes of Sn—O bonds, which agree with those reported in the literature [41]. This behavior of Sn during the electrochemical synthesis could be interesting for the fabrication of gas sensors, which commonly use Pt microelectrode and anode materials for Ni-ion batteries.

3.4 Electrodeposition of Sn

Sn electrodeposition process was performed for 1 h onto copper electrodes from EG solutions with and without NaCl. SEM images and XRD pattern were obtained on the copper surface to study the surface morphology, composition, and crystalline structure. The use of copper as electrode for the massive electrodeposition in this work is because it is much cheaper and more convenient for surface characterization of the samples than other electrode materials such as Pt and Au, which render a similar behavior in terms kinetics and morphology (metal–metal interactions). Moreover, Sn and Sn−Cu alloys are also interested in many industrial sectors

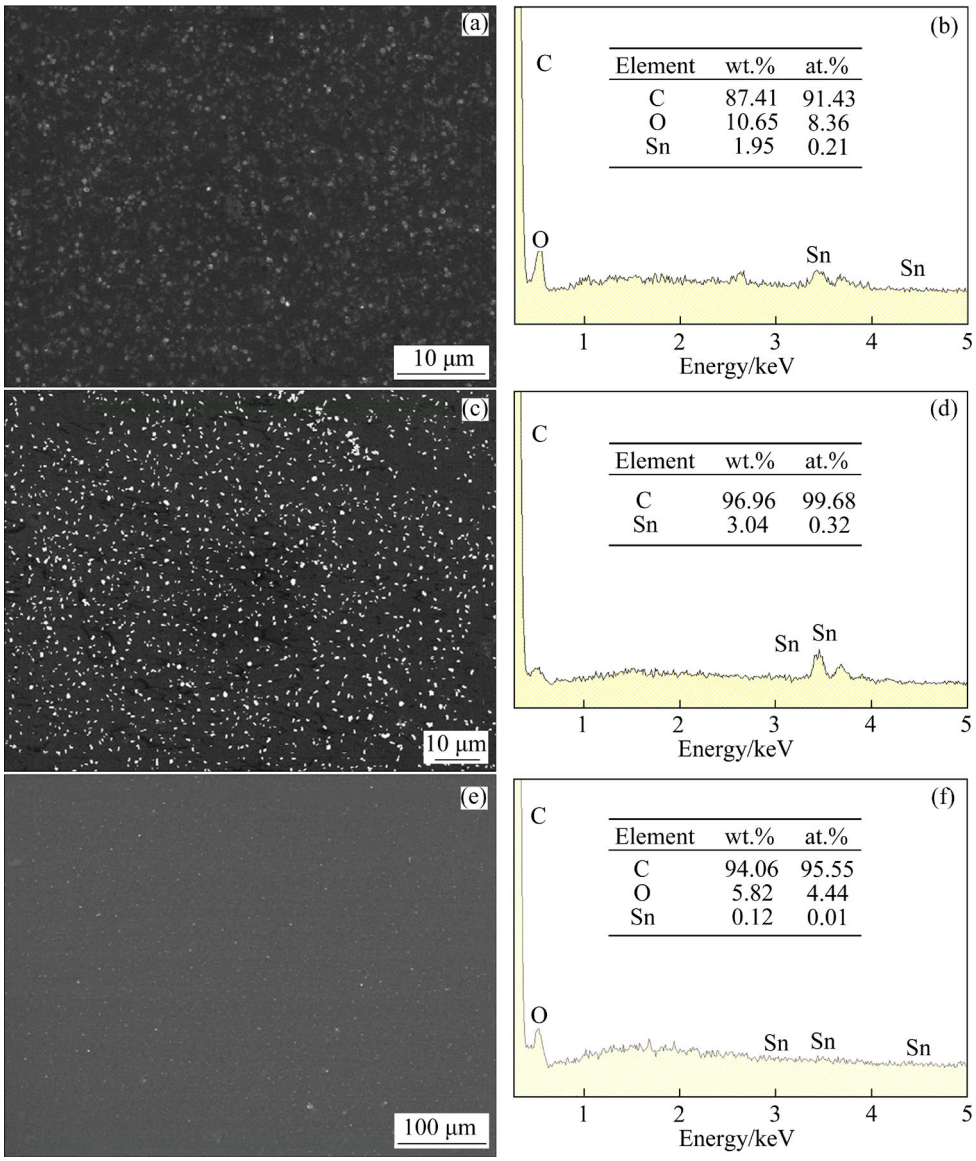

Fig. 12 EDX spectra obtained on GCE surface after Sn electrodeposition in EG for 40 s from 50 mmol/L Sn(II) with NaCl at −0.69 V (a, b) and without NaCl at −1.0 V (c, d), and in 1 mol/L HCl solution (e, f)

such as microelectronics, printed circuit boards, batteries (i.e., anode for rechargeable Li-ion battery), among others. Therefore, a study on characteristics of the Sn electrodeposition on copper electrodes is of vital importance.

Figure 13 shows SEM images and XRD pattern of Sn on the copper electrode electrodeposited for 1 h at room temperature and applied potentials (−0.69 and −0.72 V) from 50 mmol/L Sn(II) in EG with NaCl. At potentials of −0.69 and −0.72 V, the Sn deposit exhibits a compact structure with high crystallinity (see Figs. 13(a, b)). More crystalline and round grains have been observed at larger potentials (−0.72 V). In addition, the formation of Sn nanoparticles on the grain surface from Fig. 13(c) could correspond to the tin oxide or hydroxide layer due to the presence of the supporting electrolyte.

The appearance of the strong Cu peak intensity at 2θ of ~75° in XRD pattern of Fig. 13(d) could be explained due to the preferred grains orientation of the copper substrate, which could be interesting for a future study on its influence on characteristics and properties of the electrodeposited metal. Meanwhile, in this context, the bulk electrodeposition of Sn from the EG with and without NaCl presents significant differences in the morphology. Hence, in Fig. 13 Sn deposits with NaCl form a dense structure with (round) crystalized grains, while a dendrite structure with an orientation perpendicular

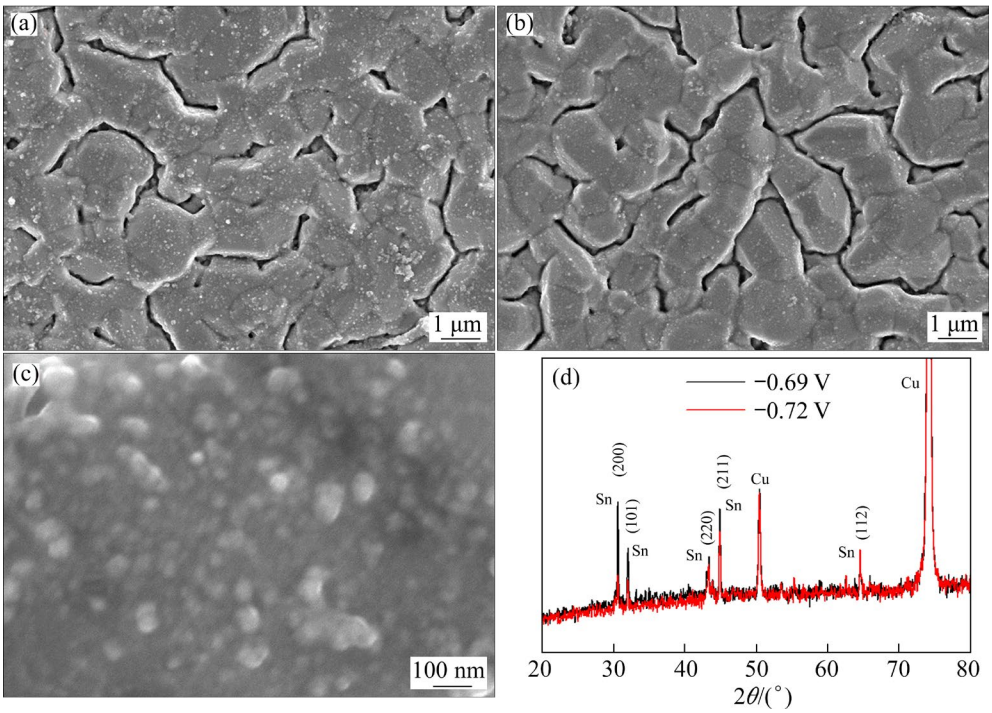

Fig. 13 SEM images (a−c) and XRD pattern (d) of Sn electrodeposited on copper electrode for 1 h at room temperature from 50 mmol/L Sn(II) in EG with NaCl at −0.69 V (a, c) and −0.72 V (b)

to the electrode surface is observed for the Sn deposit from Sn(II) in EG (without NaCl) as shown in Fig. 14. This dendritic morphology of the Sn electrodeposition is also obtained in aqueous media as reported in Ref. [28]. The formation of the dendrite structure has been explained essentially due to energetical favor along crystallographic directions during diffusion-controlled process [34,42].

The texture coefficients, TC, for each of five diffraction peaks of the Sn deposits obtained from EG, EG with NaCl, and 1 mol/L HCl solutions were calculated from their intensities relative to each other and to the standard powder pattern (ICSD No. 81157), as given in Eq. (19) [43]:

$$\mathrm{TC}(hkl)_i = \frac{I(hkl)_i / I_0(hkl)_i}{\frac{1}{N}\sum_{j=1}^{N} I(hkl)_j / I_0(hkl)_j} \quad (19)$$

where $\mathrm{TC}(hkl)_i$ is the texture coefficient for the ith reflection, $I(hkl)_i$ is the intensity in the Sn electrodeposited sample, $I_0(hkl)_i$ is the intensity in the XRD pattern, and N is the number of reflections present in the XRD pattern. The calculated $\mathrm{TC}(hkl)_i$ values are shown in Table 3.

From Table 3, there is a preferred orientation on (211) plane for both Sn deposits from EG and EG with NaCl as indicated by the high TC value for this reflection, while (101) and (112) are predominant in 1 mol/L HCl solution.

Moreover, the thickness of the Sn deposit layer in the absence of the NaCl is larger than that in the presence of NaCl, since Sn peaks in XRD pattern exhibit higher intensity than the Cu ones. This can be due to the higher applied potential required to electrodeposit Sn from EG solution without NaCl. It should be noticed that the deposited film includes two layers: the bottom part is thin film, while the upper part is dendritic morphology as seen from Fig. 14(e).

XRD pattern in Fig. 14(f) (pattern card ICSD ID 81157) indicated only two metallic phases, corresponding to Sn and Cu substrates. No other peaks were discovered, suggesting that the main phase of the electrodeposition is the pure Sn crystallizing in the tetragonal lattice.

It is important to note that when compared to the XRD pattern of samples in Fig. 13, the presence of diffraction peaks associated with SnO_2, as presented above, is not evident (even from aqueous solvent, see Fig. S5(b) in Supplementary Materials), because this thin layer is insignificant to be detected by XRD technique, which requires relatively high concentration of the compound. This is corroborated

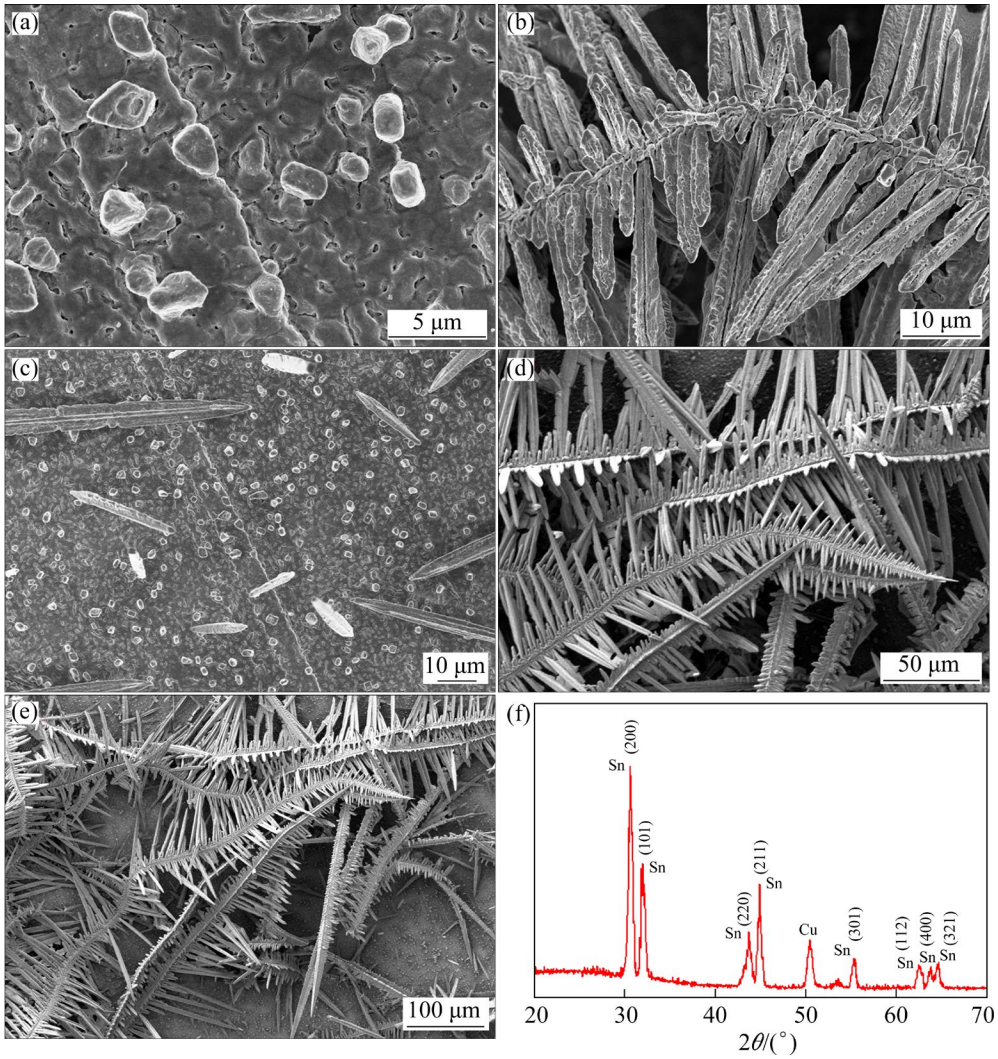

Fig. 14 SEM images (a−e) and XRD pattern (f) of Sn electrodeposited on copper electrode from 50 mmol/L Sn(II) in EG without NaCl at −1 V and room temperature for 1 h

Table 3 Texture coefficients of several planes for Sn electrodeposited on Cu substrates from different media at different applied potentials

Diffraction peak	Texture coefficient			
	EG (φ=−1 V)	EG with NaCl (φ=−0.69 V)	EG with NaCl (φ=−0.72 V)	1 mol/L HCl (φ=−0.69 V)
(200)	0.72	0.34	0.19	0.03
(101)	0.94	0.53	0.40	1.51
(220)	0.54	0.58	0.59	0.09
(211)	2.03	1.90	1.72	0.83
(112)	0.77	1.65	1.99	1.90

by the small peak intensities of Raman spectrum of Sn deposit observed in Fig. S4 in Supplementary Materials. Finally, the use of EG solutions allows to produce pure metallic Sn with more compact structure than aqueous solvent (see Fig. S5(a)) in Supplementary Materials, demonstrating that EG is a good candidate for Sn electrodeposition with better quality. It is important to note that Sn coating on copper substrates keeps the metallic luster in long time as well as good aherence on the substrate,

showing outstanding property for corrosion resistance. Moreover, the fast kinetics and easy filling of Sn electrodeposition facilitate its applications in many engineering fields such as gas sensor with complex geometry of the substrates and/or electrocatalyst, anode material for Na-ion batteries.

4 Conclusions

(1) Mechanisms and kinetics of Sn deposits from EG-based nonaqueous solvents were thoroughly studied and compared with aqueous one (1 mol/L HCl solution) using electrochemical methods. From CV curves, the reduction peaks shifted towards more positive potentials with the increase of the temperature, which thermodynamically favored the Sn electrodeposition process from EG solutions. From CA analyses, it was identified that the model, comprising two contributions, namely, 3D nucleation and diffusion-controlled growth and water reduction, was suitable to describe the early stage of the Sn electrodeposition process. The similar behavior of the CA curves obtained in aqueous system (1 mol/L HCl) corroborated the validity of the proposed model. The effect of side reaction during the Sn electrodeposition was corroborated by Raman spectroscopy, which revealed that small peak intensities were associated with a thin layer of SnO_2 formed because of water during the Sn electrodeposition.

(2) Using the model, some kinetic parameters such as A, N_0, and D were determined for each temperature. It has been verified that the D value of Sn(II) in EG with NaCl is proportional to the reciprocal of the temperature. The temperature-dependent analysis of the diffusion coefficient, D, derived from CV curves allowed us to estimate the activation energy for Sn(II) bulk diffusion in EG during the Sn electrodeposition.

(3) SEM images taken on the electrode surface, EDS, and XRD verified the formation of highly crystallized Sn grains and dendrite structures with and without supporting electrolyte, respectively. Based on texture coefficients calculated from XRD spectra, there was a preferred orientation on (211) plane for both Sn deposits from EG and EG with supporting electrolyte, while (101) and (112) planes are predominant in 1 mol/L HCl solution. The excellent quality of the Sn deposit verified the use of EG solutions as a potential solvent for metal electrodeposition, synthesis of electrocatalysts and other industrial sectors such as microelectronics, printed circuit boards, and batteries.

CRediT authorship contribution statement

Kiem Van DO: Data curation, Format analysis, Investigation, Writing − Review & editing; **Hieu Van NGUYEN:** Format analysis, Investigation, Writing − Review & editing; **Tu Manh LE:** Conceptualization, Investigation, Format analysis, Methodology, Supervision, Writing − Review & editing.

Declaration of competing interest

The authors declare that they have no known competing financial interests or personal relationships that could have appeared to influence the work reported in this paper.

Acknowledgments

This work has been supported by the Phenikaa Innovation Foundation, Vietnam (No. ĐMST.2022.01).

Supplementary Materials

Supplementary Materials in this paper can be found at: http://tnmsc.csu.edu.cn/download/23-p2714-2023-0382-Supplementary_Materials.pdf.

References

[1] DEAN R R, THWAITES C J. Tinplate and tin coating technology [J]. Journal of Metals, 1987, 39: 42−45.

[2] AN Xiao-wei, LI Sha-sha, YOSHIDA A, WANG Zhong-de, HAO Xiao-gang, ABUDULA A, GUAN Guo-qing. Electrodeposition of tin-based electrocatalysts with different surface tin species distributions for electrochemical reduction of CO_2 to HCOOH [J]. ACS Sustainable Chemistry & Engineering, 2019, 7(10): 9360−9368.

[3] ALIZADEH M, TEYMURI A. Structure, indentation and corrosion characterizations of high-silicon Ni−Si nano-composite coatings prepared by modified electrodeposition process [J]. Transactions of Nonferrous Metals Society of China, 2019, 29(3): 608−616.

[4] YOUSEFI E, IRANNEJAD A, SHARAFI S. Electrodeposition and characterization of nanocrystalline Fe−Ni−Cr alloy coatings synthesized via pulse current method [J]. Transactions of Nonferrous Metals Society of China, 2019, 29(12): 2591−2603.

[5] TRAN K D, NGUYEN V T, CHU M H, NGUYEN V D, NGUYEN N V, LE V T, NGUYEN T S, NGUYEN V H, LE M T. Investigation of zinc electronucleation and growth mechanisms onto platinum electrode from a deep eutectic solvent for gas sensing applications [J]. Journal of Applied Electrochemistry, 2022, 52: 299−309.

[6] LE M T, ARCE-ESTRADA E M, MEJÍA-CABALLERO I, ALDANA-GONZÁLEZ J, ROMERO-ROMO M, PALOMAR-PARDAVÉ M. Electrochemical synthesis of cobalt with different crystal structures from a deep eutectic solvent [J]. Journal of the Electrochemical Society, 2018, 165(7): 285−290.

[7] ABEDINI B, PARVINI AHMADI N, YAZDANI S, MAGAGNIN L. Electrodeposition and corrosion behavior of Zn−Ni−Mn alloy coatings deposited from alkaline solution [J]. Transactions of Nonferrous Metals Society of China, 2020, 30(2): 548−558.

[8] XUE Jian-rong, ZHONG Hong, WANG Shuai, LI Chang-xin, WU Fang-fang. Influence of sodium silicate on manganese electrodeposition in sulfate solution [J]. Transactions of Nonferrous Metals Society of China, 2016, 26(4): 1126−1137.

[9] FASHU S, GU Chang-dong, ZHANG Jia-lei, HUANG Mei-ling, WANG Xiu-li, TU Jiang-ping. Effect of EDTA and NH_4Cl additives on electrodeposition of Zn−Ni films from choline chloride-based ionic liquid [J]. Transactions of Nonferrous Metals Society of China, 2015, 25(6): 2054−2064.

[10] LIU Ai-min, GUO Meng-xia, SHI Zhong-ning, LIU Yu-bao, LIU Feng-guo, HU Xian-wei, YANG You-jian, TAO Wen-ju, WANG Zhao-wen. Physicochemical properties of 1,3-dimethyl-2-imidazolinone−$ZnCl_2$ solvated ionic liquid and its application in zinc electrodeposition [J]. Transactions of Nonferrous Metals Society of China, 2021, 31(3): 832−841.

[11] SALOMÉ S, PEREIRA N M, FERREIRA S E, PEREIRA M C, SILVA F A. Tin electrodeposition from choline chloride based solvent: Influence of the hydrogen bond donors [J]. Journal of Electroanalytical Chemistry, 2013, 703: 80−87.

[12] ANICAI L, PETICA A, COSTOVICI S, PRIOTEASA P, VISAN T. Electrodeposition of Sn and NiSn alloys coatings using choline chloride based ionic liquids—Evaluation of corrosion behavior [J]. Electrochimica Acta, 2013, 114: 868−877.

[13] SHAH D, MJALLI S F. Effect of water on the thermo-physical properties of Reline: An experimental and molecular simulation based approach [J]. Physical Chemistry Chemical Physics, 2014, 16: 23900−23907.

[14] YADAV A, PANDEY S. Densities and viscosities of (choline chloride + urea) deep eutectic solvent and its aqueous mixtures in the temperature range 293.15 K to 363.15 K [J]. Journal of Chemical & Engineering Data, 2014, 59(7): 2221−2229.

[15] CHERIGUI E, SENTOSUN K, MAMME H M, LUKACZYNSKA-ANDESON M, TERRYN H, BALS S, USTARROZ J. On the control and effect of water content during the electrodeposition of Ni nanostructures from deep eutectic solvents [J]. The Journal of Physical Chemistry C, 2018, 122(40): 23129−23142.

[16] LUKACZYNSKA-ANDERSON M, MAMME H M, CEGLIA A, BERGH K, STRYCKER J, PROFT F, TERRYN H, USTARROZ J. The role of hydrogen bond donor and water content on the electrochemical reduction of Ni^{2+} from deep eutectic solvents—An experimental and modelling study [J]. Physical Chemistry Chemical Physics, 2020, 22(28): 16125−16135.

[17] MAJIDZADE A V, ALIYEV S A, ELROUBY M, BABANLY M D, TAGIYEV D. Electrodeposition and growth of iron from an ethylene glycol solution [J]. Acta Chimica Slovenica,2021, 68(1): 185−192.

[18] BERNASCONI R, FIRTIN G F, KAHYAOGLU B, NOBILI L, MAGAGNIN L. Electrodeposition of zinc-nickel alloys from ethylene glycol for corrosion protection [J]. ECS Meeting Abstracts, 2021, 18: 799−799.

[19] PANZERI G, ACCOGLI A, GIBERTINI E, RINALDI C, NOBILI L, MAGAGNIN L. Electrodeposition of high-purity nanostructured iron films from Fe(II) and Fe(III) non-aqueous solutions based on ethylene glycol [J]. Electrochimica Acta, 2018, 271: 576−581.

[20] PANZERI G, ACCOGLI A, GIBERTINI E, VAROTTO S, RINALDI C, NOBILI L, MAGAGNIN L. Electrodeposition of cobalt thin films and nanowires from ethylene glycol-based solution [J]. Electrochemistry Communications, 2019, 103: 31−36.

[21] PHI T L, NGUYEN T S, NGUYEN V H, PALOMAR-PARDAVÉ M, MORALES-GIL P, LE M T. Insights into electronucleation and electrodeposition of nickel from a non-aqueous solvent based on $NiCl_2{\cdot}6H_2O$ dissolved in ethylene glycol [J]. Inorganic Chemistry, 2022, 61: 5099−5111.

[22] VOROBYOVA N T, KUDAKA A A. Electrodeposition of Ni–Sn alloy from ethylene glycol electrolyte. Part 1: Cathodic reactions [J]. Transactions of the IMF, 2022, 100(1): 36−42.

[23] MALTANAVA M H, VOROBYOVA N T, VRUBLE-VSKAYA N O. Electrodeposition of tin coatings from ethylene glycol and propylene glycol electrolytes [J]. Surface and Coatings Technology, 2014, 254: 388−397.

[24] PAN Chong-gen, MAO Jiang-hong, JIN Wei-liang, FAN Wei-jie, ZHU Da-yong. Effects of environmental Water-Level changes and bidirectional electromigration rehabilitation on durability of concrete [J]. Construction and Building Materials, 2020, 265(5): 120335.

[25] VIEIRA L, BURT J, RICHARDSON W P, SCHLOFFER D, FUCHS D, MOSER A, BARTLETT N P, REID G, GOLLAS R B. Tin, bismuth, and tin-bismuth alloy electrodeposition from chlorometalate salts in deep eutectic solvents [J]. ChemistryOpen, 2017, 6: 393−401.

[26] ROSOIU P S, COSTOVICI S, MOISE C, PETICA A, ANICAI L, VISAN T, ENACHESCU M. Electrodeposition of ternary Sn−Cu−Ni alloys as lead-free solders using deep eutectic solvents [J]. Electrochimica Acta, 2021, 398: 139339.

[27] CAO Hua-zhen, HU Li-long, ZHANG Hui-bin, HOU Guang-ya, TANG Yi-ping, ZHENG Guo-qu. The significant effect of supporting electrolytes on the galvanic deposition of metallic rhenium [J]. International Journal of Electrochemical Science, 2020, 15: 6769−6777.

[28] WALSH C F, LOW T J C. A review of developments in the electrodeposition of tin [J]. Surface and Coatings Technology, 2016, 288: 79−94.

[29] IBRAHIM M, RADADI R. Role of glycine as a complexing agent in nickel electrodeposition from acidic sulphate bath [J]. International Journal of Electrochemical Science, 2015, 10: 4946−4971.

[30] BERZINS T, DELAHAY P. Oscillographic polarographic waves for the reversible deposition of metals on solid electrodes [J]. Journal of the American Chemical Society, 1953, 75: 555−559.
[31] PALOMAR-PARDAVÉ M, SCHARIFKER R B, ARCE M E, ROMERO-ROMO M. Nucleation and diffusion-controlled growth of electroactive centers: Reduction of protons during cobalt electrodeposition [J]. Electrochimica Acta, 2005, 50: 4736−4745.
[32] SCHARIFKER B, HILLS G. Theoretical and experimental studies of multiple nucleation [J]. Electrochimica Acta, 1983, 28: 879−889.
[33] SCHARIFKER R B, MOSTANY J. Three-dimensional nucleation with diffusion-controlled growth: Part I. Number density of active sites and nucleation rates per site [J]. Journal of Electroanalytical Chemistry and Interfacial Electrochemistry, 1984, 177: 13−23.
[34] CAO Ling, LIU Jun, HUANG Wei, LI Ze-lin. Facile fabrication of superhydrophobic surfaces on zinc substrates by displacement deposition of Sn [J]. Applied Surface Science, 2013, 265: 597−602.
[35] PALOMAR-PARDAVÉ M, ALDANA-GONZÁLEZ J, BOTELLO E L, ARCE-ESTRADA M E, RAMÍREZ-SILVA T M, MOSTANY J, ROMERO-ROMO M. Influence of temperature on the thermodynamics and kinetics of cobalt electrochemical nucleation and growth [J]. Electrochimica Acta, 2017, 241: 162−169.
[36] BAKKALI S, CHERKAOUI M, BOUTOUIL A, LAAMARI R M, TOUHAMI M E, BELFAKIR M, ZARROUK A. Theoretical and experimental studies of tin electrodeposition [J]. Surfaces and Interfaces, 2020, 19: 100480.
[37] SOLIMAN M A H. Formalin solution and acetone as organic additives in electrodeposition of copper [J]. Applied Surface Science, 2002, 195(1/2/3/4): 155−165.
[38] ISAEV V A, GRISHENKOVA O V, ZAYKOV Y P. On the theory of 3D multiple nucleation with kinetic controlled growth [J]. Journal of Electroanalytical Chemistry, 2018, 818: 265−269.
[39] MYLAND C J, OLDHAM B K. Cottrell's equation revisited: An intuitive, but unreliable, novel approach to the tracking of electrochemical diffusion [J]. Electrochemistry Communications, 2004, 6(4): 344−350.
[40] LOBO M M V. Mutual diffusion coefficients in aqueous electrolyte solutions [J]. Pure and Applied Chemistry, 1993, 65(12): 2613−2640.
[41] LAVANYA N, SEKAR C, FAZIO E, NERI F, LEONARDI G, NERI G. Development of a selective hydrogen leak sensor based on chemically doped SnO_2 for automotive applications [J]. International Journal of Hydrogen Energy, 2017, 42(15): 10645−10655.
[42] QIN Yao, SONG Yin, SUN Ni-juan, ZHAO Na-na, LI Mei-xian, QI Li-min. Ionic liquid-assisted growth of single-crystalline dendritic gold nanostructures with a three-fold symmetry [J]. Chemistry of Materials, 2008, 20: 3965−3972.
[43] MAAZ K, KARIM S, USMAN M, MUMTAZ A, LIU J, DUAN L J, MAQBOOL M. Effect of crystallographic texture on magnetic characteristics of cobalt nanowires [J]. Nanoscale Research Letters, 2010, 5: 1111−1117.

含 Sn(II)乙二醇溶液中 Sn 的形核和生长：电化学行为和温度效应

Kiem Van DO[1], Hieu Van NGUYEN[1,2], Tu Manh LE[2,3]

1. Faculty of Electrical and Electronic Engineering, Phenikaa University, Yen Nghia, Ha-Dong, Hanoi 10000, Vietnam;
2. Phenikaa Research and Technology Institute (PRATI), A&A Green Phoenix Group, 167 Hoang Ngan, Hanoi 10000, Vietnam;
3. Faculty of Materials Science and Engineering, Phenikaa Institute for Advanced Study (PIAS), Phenikaa University, Hanoi 10000, Vietnam

摘　要：将 $SnCl_2·2H_2O$ 溶解到乙二醇溶液中，研究 Sn 在玻璃碳电极上形核和生长过程的热力学和动力学。从伏安图中观察到的典型还原和氧化峰证明了乙二醇溶液电沉积 Sn 的能力。从动电位和恒电位研究中得出的扩散系数值具有温度依赖性，这有助于确定和验证估算的 Sn(II)体扩散激活能。计时电流法的研究结果表明，描述 Sn 电沉积早期阶段的合适模型可能包括 Sn 的三维形核、受扩散控制的生长以及水还原的贡献，该模型通过理论和实验方法得到了适当的验证。并通过该模型确定了典型的动力学参数，包括形核率(A)、Sn 核的数密度(N_0)和扩散系数(D)。使用 SEM、EDX 和 XRD 技术验证了高质量 Sn 核的存在及其结构。

关键词：Sn；形核；生长；乙二醇；形核动力学；电沉积

(Edited by Wei-ping CHEN)